Journal of Fluids and Structures (2000) **14,** 1013–1034
doi:10.1006/jfls.2000.0306, available online at http://www.idealibrary.com on IDEAL®

HYDRODYNAMIC INTERACTIONS AMONG A GREAT NUMBER OF COLUMNS SUPPORTING A VERY LARGE FLEXIBLE STRUCTURE

M. KASHIWAGI

Research Institute for Applied Mechanics, Kyushu University
Kasuga, Fukuoka 816-8580, Japan

(Received 21 January 1999, and in final form 20 April 2000)

A hierarchical interaction theory is presented, which can treat hydrodynamic interactions among a great number of bodies rigorously in the framework of linear potential theory. After checking numerical accuracy and convergence for a square array of 64 half-immersed spheres, the theory is applied to column-supported structures with 1280, 2880, and 5120 equally spaced circular cylinders as supporting columns. With the computed hydrodynamic and hydrostatic forces, the motion equation of an upper deck is solved using the mode-expansion method. Trapped-wave phenomena among a large number of columns are observed at relatively short waves, and numerical examples of those effects on the elastic deflection of the upper deck and the wave pattern around column-supported structures are also shown.

1. INTRODUCTION

VERY LARGE FLOATING STRUCTURES (VLFSs) are being considered for use as floating airports, storage, and manufacturing facilities. Those VLFSs are categorized according to the configuration under the sea level into: (i) a pontoon-type VLFS, having a box-shaped structure with very shallow draft, and (ii) a column-supported-type VLFS, consisting of a thin upper deck and a great number of buoyancy elements.

A number of studies have been made on the pontoon-type VLFS; e.g. Ohmatsu (1997), Kashiwagi (1998), Lin & Takaki (1998), and others cited therein. However, it may not be the case that pontoon-type structures are overwhelmingly advantageous. In fact, Kagemoto (1995) reported some engineering aspects in favour of a column-supported structure, under the assumption of the same flexural rigidity in both types of structure. His study was largely based on an approximate analysis, and therefore more careful study is needed using a rigorous but efficient numerical method.

In the case of column-supported-type VLFS, besides the upper deck being flexible due to its relatively small rigidity, hydrodynamic interactions among a great number of columns are important in evaluating the diffraction and radiation forces. It is said that the number of columns could exceed 10 000, and the conventional calculation methods cannot be used owing to the huge amount of computer memory and computation time required.

In order to surmount this difficulty, a new hierarchical interaction theory is developed in this paper, which is regarded as an extension of Kagemoto & Yue's (1986) interaction theory. No matter how many columns are used, the present theory can be applied with reasonable computation time, and hydrodynamic interactions can be taken into account rigorously in the framework of linearized potential theory. In the hierarchical scheme,

0889–9746/00/101013 + 22 $35.00/0

a great number of actual columns are grouped into several fictitious bodies and the fictitious bodies are grouped further into a certain number of larger fictitious bodies. This procedure can be repeated up to any hierarchical level, if necessary. The interactions are then considered at each level, and information on interactions can be transmitted upward or downward as required.

The elastic deflection of an upper deck is represented by a superposition of modal functions. Then, the hydrodynamic forces acting on supporting columns in response to specified modes of the deck are computed by the hierarchical interaction theory. With the computed hydrodynamic and hydrostatic forces, the amplitude of each modal function is determined by solving the motion equation of the deck by means of a Galerkin scheme.

Recently, Murai *et al.* (1998) independently developed almost the same theory and conducted some pilot computations. However, the contributions of evanescent wave components were ignored at the outset, and the motion equation of the deck was solved in a different way: that is, firstly the elastic deflection of the deck was represented by a succession of rigid-body vertical motions of small substructures; and then coupled equations of motion of the substructures were solved, with hydrodynamic and structural interactions taken into account. Their investigation seems not to extend to the effect of resonant interactions among many columns whose number is of a realistic order of several thousands.

In connection with hydrodynamic interactions, some researchers have recently studied trapped wave phenomena among a certain number of cylinders; e.g. Yoshida *et al.* (1994), Maniar & Newman (1997), Evans & Porter (1997), and Utsunomiya & Eatock Taylor (1998). According to these studies, trapped wave phenomena occur at some specific frequencies when the wavelength is of the same order as the distance between the centrelines of adjacent cylinders. This wavelength may be short for a realistic column-supported VLFS but must be studied, because these phenomena may cause detrimental effects on elastic responses of the upper deck. The present paper provides computations for these phenomena, including the wave pattern around column-supported-type structures with 1280 and 5120 equally spaced circular cylinders.

2. FORMULATION

We consider a column-supported VLFS, comprising of a thin deck and a great number of buoyancy columns. The deck is rectangular in plan, with length L and width B. Theoretically, the geometry and arrangement of elementary columns can be arbitrary, but in this paper identical and equally spaced columns are considered and each column is a truncated circular cylinder with radius a and draft d. The centrelines of adjacent cylinders are separated by a distance $2s$ in both x- and y-axis of a Cartesian coordinate system, where $z = 0$ is the plane of the undisturbed free surface and the water depth is constant at $z = h$ (see Figure 1). Incident plane waves propagate in the direction with angle β relative to the x-axis. In addition to the global coordinate system, we shall use a local cylindrical coordinate system (r_j, θ_j, z), with the origin placed at $(x_j, y_j, 0)$, i.e. the centre of the jth cylinder.

Time-harmonic motions of small amplitude are considered, with the complex time dependence $e^{i\omega t}$ applied to all first-order oscillatory quantities. The boundary conditions on the body and free surface are linearized, and potential flow is assumed.

We then express the velocity potential, governed by Laplace's equation, in the form

$$\Phi(x, y, z) = \frac{gA}{i\omega}\{\Phi_I(x, y, z) + \Phi_S(x, y, z)\} + \sum_{k=1}^{\infty} i\omega X_k \Phi_k(x, y, z), \tag{1}$$

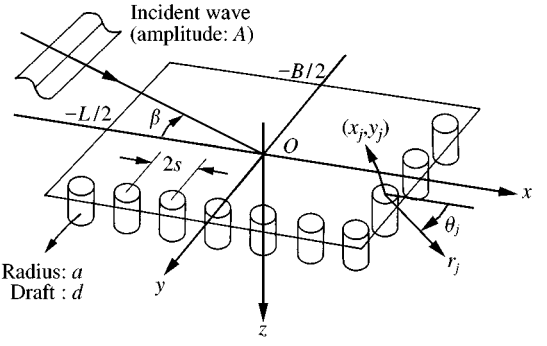

Figure 1. Coordinate system and notations.

where A is the amplitude of an incident wave, ω is the circular frequency, and g is the gravitational acceleration.

Φ_I is the incident-wave velocity potential, which is given by

$$\Phi_I = Z_0(z)\,\mathrm{e}^{-\mathrm{i}\,k_0(x\cos\beta + y\sin\beta)}, \tag{2}$$

where

$$Z_0(z) = \frac{\cosh k_0(z-h)}{\cosh k_0 h}, \quad k_0 \tanh k_0 h = \frac{\omega^2}{g} \equiv K. \tag{3}$$

Φ_S in equation (1) represents the scattered potential and the sum, $\Phi_I + \Phi_S = \Phi_D$, is referred to as the total diffraction potential.

In the radiation component, suffix k refers to the kth mode of motion, which includes not only rigid-body motions but also a set of "generalized" modes to represent elastic deflections of a deck. X_k denotes the complex amplitude of each mode.

Since the deck is very thin compared with other dimensions of the structure, it is enough to consider only the vertical deflection. This is expressed in the form

$$w(x, y) = \sum_{k=1}^{\infty} X_k\,\zeta_k(x, y) = \sum_{r=0}^{\infty}\sum_{s=0}^{\infty} X_{rs}\,u_r(x)\,v_s(y), \tag{4}$$

where the modal functions in the x- and y-axis, $u_r(x)$ and $v_s(y)$, respectively, are the natural modes for the bending of a uniform beam with free ends. Specifically, $u_r(x)$ can be written as

$$\begin{aligned} u_0(x) &= \tfrac{1}{2}, \\ u_{2r}(x) &= \frac{1}{2}\left[\frac{\cos\kappa_{2r}x}{\cos\kappa_{2r}} + \frac{\cosh\kappa_{2r}x}{\cosh\kappa_{2r}}\right], \end{aligned} \tag{5}$$

$$\begin{aligned} u_1(x) &= \tfrac{\sqrt{3}}{2}x, \\ u_{2r+1}(x) &= \frac{1}{2}\left[\frac{\sin\kappa_{2r+1}x}{\sin\kappa_{2r+1}} + \frac{\sinh\kappa_{2r+1}x}{\sinh\kappa_{2r+1}}\right]. \end{aligned} \tag{6}$$

Here the coordinate x is normalized with $L/2$ and the same implication will be used hereafter. The factors κ_r are the positive roots of the equation

$$(-1)^r \tan\kappa_r + \tanh\kappa_r = 0; \tag{7}$$

$v_s(y)$ can also be written in a similar form, with x replaced by y/b, where $b = B/L$, on the right-hand sides of equations (5) and (6).

Following the notation of Newman (1994), the normal component of the kth modal function is defined as

$$n_k = \zeta_k(x, y)\, n_z, \tag{8}$$

where n_z is the z-component of the unit normal vector pointing out of the body.

3. DIFFRACTION PROBLEM

3.1. Diffraction Characteristics of a Single Body

In the interaction theory for a large number of floating bodies, it is a prerequisite to solve the diffraction problem of the jth body in a set of "generalized" incident waves, defined by

$$\{\psi_I^j\} = \begin{Bmatrix} Z_0(z)\, \mathrm{J}_p(k_0 r_j)\, \mathrm{e}^{-\mathrm{i}p\theta_j} \\ Z_n(z)\, \mathrm{I}_p(k_n r_j)\, \mathrm{e}^{-\mathrm{i}p\theta_j} \end{Bmatrix}, \tag{9}$$

where $p = 0, \pm 1, \pm 2, \ldots, \pm \infty$, $n = 1, 2, \ldots, \infty$, and

$$Z_n(z) = \frac{\cos k_n(z - h)}{\cos k_n h}, \quad k_n \tan k_n h = -K. \tag{10}$$

J_p and I_p in equation (9) denote the first kind of Bessel and modified Bessel functions, respectively.

The above diffraction problem can be solved with, for instance, the boundary-element method as shown in Appendix A, and the resulting scattered potentials can be written in the form

$$\{\varphi_S^j\} = [B_j]^{\mathrm{T}} \{\psi_S^j\}, \tag{11}$$

where

$$\{\psi_S^j\} = \begin{Bmatrix} Z_0(z)\, \mathrm{H}_m^{(2)}(k_0 r_j)\, \mathrm{e}^{-\mathrm{i}m\theta_j} \\ Z_n(z)\, \mathrm{K}_m(k_n r_j)\, \mathrm{e}^{-\mathrm{i}m\theta_j} \end{Bmatrix}, \tag{12}$$

with $m = 0, \pm 1, \pm 2, \ldots, \pm \infty$, and $n = 1, 2, \ldots, \infty$. $\mathrm{H}_m^{(2)}$ and K_m are the second kind of Hankel and modified Bessel functions, respectively. $[B_j]^{\mathrm{T}}$ denotes the transpose of the matrix $[\mathrm{B}_j]$. This coefficient matrix, $[B_j]$, is referred to as the diffraction characteristics matrix of the jth body.

Wave forces in response to the "generalized" waves may be computed at the same time, and expressed in the form

$$\{E_z^j\} = \iint_{S_j} \{\psi_I^j + \varphi_S^j\} n_z \, \mathrm{d}S = \iint_{S_j} \{\varphi_D^j\} n_z \, \mathrm{d}S, \tag{13}$$

where S_j denotes the surface of the jth body below $z = 0$.

3.2. Hierarchical Interaction Theory

We consider a rectangular array of identical and equally spaced columns, but for convenience of explanation, only a schematic arrangement of bodies is shown in Figure 2. The

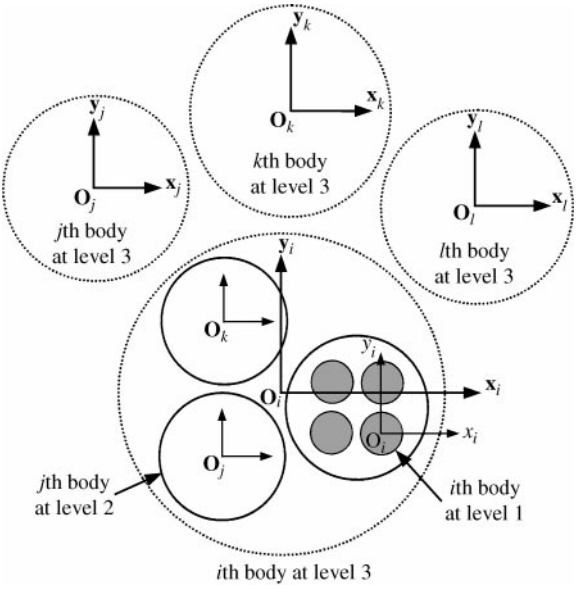

Figure 2. Coordinate systems in hierarchical interaction theory.

shaded bodies in Figure 2 are actual bodies, which are referred to as bodies at level one. A number of level-one bodies are grouped to form a fictitious body, which is at level two, and several fictitious bodies are grouped further to form a bigger fictitious body at level three. Repeating this hierarchical treatment makes it possible to view the interactions among a large number of bodies as a succession of simpler interactions due to smaller number of bodies. To explain the theory, it may be enough to consider only two hierarchical levels, i.e. $\ell = 2$ would correspond to the highest level in this case.

Rewriting the incident-wave potential in terms of a polar coordinate system of a fictitious body i at level ℓ, we obtain the following:

$$\Phi_I = \alpha_i(k_0, \beta) \sum_{p=-\infty}^{\infty} \mathrm{e}^{\mathrm{i}p(\beta-\pi/2)} \{ Z_0(z) \mathrm{J}_p(k_0 r_i) \mathrm{e}^{-\mathrm{i}p\theta_i} \}, \tag{14}$$

where

$$\alpha_i(k_0, \beta) = \mathrm{e}^{-\mathrm{i}k_0(x_i \cos\beta + y_i \sin\beta)}. \tag{15}$$

With the vector of generalized incident waves defined by equations (9), (14) can be expressed in the form

$$\Phi_I = \{ a^i \}^{\mathrm{T}} \{ \psi_I^i \}, \tag{16}$$

where $\{a^i\}$ is a vector of coefficients defined by means of equation (14).

According to the Kagemoto & Yue (1986) interaction theory, scattered waves due to other bodies must be viewed as incident waves upon the body under consideration. Thus, utilizing the coordinate transformation matrix, $[T_{ij}]$ given in Appendix B, the total

incident-wave potential on body i at level ℓ is written as

$$\phi^i_{I,\ell} = \left(\{a^i\}^{\mathrm{T}} + \sum_{\substack{n=1 \\ n \neq i}}^{N_\ell} \{A^n_{S,\ell}\}^{\mathrm{T}} [T^\ell_{ni}] \right) \{\psi^i_{I,\ell}\}, \tag{17}$$

where N_ℓ is the number of fictitious bodies at level ℓ and $\{A^i_{S,\ell}\}$ is the vector of unknown coefficients of the scattered potential due to body i.

Assuming that the diffraction characteristics of a fictitious body i at level ℓ are obtained and expressed with the matrix $[\mathscr{B}_{i,\ell}]$, the following relation can be established:

$$\begin{aligned} \phi^i_{S,\ell} &= \left(\{a^i\}^{\mathrm{T}} + \sum_{\substack{n=1 \\ n \neq i}}^{N_\ell} \{A^n_{S,\ell}\}^{\mathrm{T}} [T^\ell_{ni}] \right) [\mathscr{B}_{i,\ell}]^{\mathrm{T}} \{\psi^i_{S,\ell}\} \\ &= \{A^i_{S,\ell}\}^{\mathrm{T}} \{\psi^i_{S,\ell}\}. \end{aligned} \tag{18}$$

One can therefore obtain a linear set of equations for determining the unknown coefficients, $\{A^i_{S,\ell}\}$, in the form

$$\{A^i_{S,\ell}\} - [\mathscr{B}_{i,\ell}] \sum_{\substack{n=1 \\ n \neq i}}^{N_\ell} [T^\ell_{ni}]^{\mathrm{T}} \{A^n_{S,\ell}\} = [\mathscr{B}_{i,\ell}] \{a^i\}, \quad i = 1 \sim N_\ell. \tag{19}$$

In reality, however, the matrix $[\mathscr{B}_{i,\ell}]$ is also unknown at this stage, because the level ℓ is fictitious. To determine this matrix, the diffraction problem of a fictitious body for the components of generalized incident waves, $\{\psi^i_{I,\ell}\}$, needs to be considered.

A fictitious body at level ℓ includes $N_{\ell-1}$ bodies at level $\ell - 1$ (which are actual bodies here). Thus we must consider again the interactions among these bodies. The local (downward) expansion of $\{\psi^i_{I,\ell}\}$ about the origin of body j at level $\ell - 1$ can be found in Appendix B. Then, as in equation (17), the total incident-wave potential on body j at level $\ell - 1$ is written in the following form:

$$\{\varphi^j_{I,\ell-1}\} = \left([I^{\ell-1}_{ij}] + \sum_{\substack{n=1 \\ n \neq j}}^{N_{\ell-1}} [A^n_{S,\ell-1}]^{\mathrm{T}} [T^{\ell-1}_{nj}] \right) \{\psi^j_{I,\ell-1}\}. \tag{20}$$

Here, note that the unknown coefficients for the scattered potential, $[A^j_{S,\ell-1}]$, are given in a matrix form.

As shown in Section 3.1, the diffraction characteristics of a single body can be given by the matrix $[B_j]$, which is regarded as determined, because the level $\ell - 1$ is the lowest level. Therefore, in the same manner as in obtaining equation (19), the algebraic simultaneous equations for the coefficient matrix $[A^j_{S,\ell-1}]$ can be derived in the form

$$[A^j_{S,\ell-1}] - [B_{j,\ell-1}] \sum_{\substack{n=1 \\ n \neq j}}^{N_{\ell-1}} [T^{\ell-1}_{nj}]^{\mathrm{T}} [A^n_{S,\ell-1}] = [B_{j,\ell-1}] [I^{\ell-1}_{ij}]^{\mathrm{T}}, \quad j = 1 \sim N_{\ell-1}. \tag{21}$$

Solving equation (21) means that the diffraction problem at level $\ell - 1$ is completely solved. Thus, considering an outer-field expression of the corresponding scattered potentials of $N_{\ell-1}$ bodies, the diffraction characteristics of a fictitious body at level ℓ may be given. For that purpose, the multipole (upward) expansion of $\{\psi^j_{S,\ell-1}\}$ about the origin of body i at level ℓ must be considered, which is described also in Appendix B. Then, collecting

the contributions from all bodies inside a fictitious body, the vector of scattered potentials can be found as follows:

$$\sum_{j=1}^{N_{\ell-1}} [A^j_{S,\ell-1}]^{\mathrm{T}}\{\psi^j_{S,\ell-1}\} = \sum_{j=1}^{N_{\ell-1}} [A^j_{S,\ell-1}]^{\mathrm{T}}[M^{\ell}_{ji}]\{\psi^i_{S,\ell}\} \equiv [\mathscr{B}_{i,\ell}]^{\mathrm{T}}\{\psi^i_{S,\ell}\}. \tag{22}$$

Therefore we have

$$[\mathscr{B}_{i,\ell}] = \sum_{j=1}^{N_{\ell-1}} [M^{\ell}_{ji}]^{\mathrm{T}}[A^j_{S,\ell-1}]. \tag{23}$$

Substituting this diffraction characteristics matrix into equation (19) determines the coefficient vector of the scattered potential at level ℓ. This completes the description of the entire flow field.

3.3. Wave Exciting Force

Since fundamental wave forces due to each component of the generalized incident waves are already computed and given by equation (13), the only further requirement for computing the wave-exciting force is to find the amplitude of waves impinging upon the actual bodies at level $\ell - 1$. This can be done by simply combining equations (17) and (20), with the result

$$\phi^j_{I,\ell-1} = \{\mathscr{A}^j_D\}^{\mathrm{T}}\{\psi^j_{I,\ell-1}\}, \tag{24}$$

where

$$\{\mathscr{A}^j_D\}^{\mathrm{T}} = \left(\{a^i\}^{\mathrm{T}} + \sum_{\substack{n=1\\ n\neq i}}^{N_\ell} \{A^n_{S,\ell}\}^{\mathrm{T}}[T^{\ell}_{ni}]\right)\left([I^{\ell}_{ij}{}^{-1}] + \sum_{\substack{n=1\\ n\neq j}}^{N_{\ell-1}} [A^n_{S,\ell-1}]^{\mathrm{T}}[T^{\ell}_{nj}{}^{-1}]\right). \tag{25}$$

With this notation, the linearized pressure on body j in the diffraction problem is given by $p_D = -\rho g A\{\mathscr{A}^j_D\}^{\mathrm{T}}\{\varphi^j_D\}$. Therefore, the total wave-exciting force in the mth mode can be computed as

$$\begin{aligned} -\iint_{S_H} p_D\, n_m\, \mathrm{d}S &= \rho g A \sum_{j=1}^{N_B} \iint_{S_j} \{\mathscr{A}^j_D\}^{\mathrm{T}}\{\varphi^j_D\}\,\zeta_m(x,y)\, n_z\, \mathrm{d}S \\ &\simeq \rho g A \sum_{j=1}^{N_B} \zeta^j_m \{\mathscr{A}^j_D\}^{\mathrm{T}}\{E^j_z\} \equiv \rho g A\, E_m, \end{aligned} \tag{26}$$

where the definition of equation (8) has been used for n_m, and $\zeta^j_m = \zeta_m(x_j, y_j)$ is treated as constant on the bottom of an elementary cylinder. N_B is the total number of actual columns.

4. RADIATION PROBLEM

4.1. Radiation Characteristics of a Single Body

In the present study, since only the vertical deflection is considered, the basic solution necessary for considering hydrodynamic interactions is that of heave with unit velocity. The body boundary condition for that problem on the jth body is written as

$$\frac{\partial \Phi^j_R}{\partial n} = n_z \quad \text{on } S_j. \tag{27}$$

Several methods exist for solving this radiation problem, and a solution can be written in terms of the vector of scattered potentials defined by equation (12), in the form

$$\Phi_R^j = \{R_j\}^{\mathrm{T}}\{\psi_S^j\}. \tag{28}$$

The coefficient vector, $\{R_j\}$, is referred to as the radiation characteristics vector for a single body, which is assumed to be known.

The hydrodynamic forces computed from the above solution are the added-mass and damping coefficients. The result of this computation is written as

$$-\iint_{S_j} \Phi_R^j n_z \, \mathrm{d}S = A_{zz}^j - i B_{zz}^j. \tag{29}$$

Here A_{zz}^j and B_{zz}^j are the added mass and damping coefficients in heave, respectively, for a single body j.

4.2. Hierarchical Interaction Theory

The basic concept of the hierarchical scheme is the same as in the diffraction problem. In the radiation problem, however, let us start by considering the interactions from the lowest level. Firstly, the body boundary condition for the kth mode of motion of body i at level $\ell - 1$ can be specified as

$$\frac{\partial \Phi_{R,k}^i}{\partial n} = n_k = \zeta_k(x, y) n_z \simeq \zeta_k^i n_z. \tag{30}$$

Hence, by comparison with equation (27), the solution of $\Phi_{R,k}^i$ can be readily given by

$$\Phi_{R,k}^i = \zeta_k^i \Phi_R^i = \zeta_k^i \{R_i\}^{\mathrm{T}}\{\psi_S^i\}. \tag{31}$$

The radiated wave due to the above motion of body i may be regarded as an incident wave, when viewed from other bodies included in the same fictitious body. Taking account of interactions, the total incident-wave potential on the jth body at level $\ell - 1$ is expressed as

$$\varphi_{k,\ell-1}^j = \sum_{\substack{n=1 \\ n \neq j}}^{N_{\ell-1}} (\zeta_k^n \{R_n\}^{\mathrm{T}} + \{A_{k,\ell-1}^n\}^{\mathrm{T}})[T_{nj}^{\ell-1}]\{\psi_{I,\ell-1}^j\}. \tag{32}$$

Following the same argument as in obtaining equation (19), a linear set of equations for the unknown interaction coefficients, $\{A_{k,\ell-1}^j\}$, can be obtained in the form

$$\{A_{k,\ell-1}^j\} - [B_{j,\ell-1}] \sum_{\substack{n=1 \\ n \neq j}}^{N_{\ell-1}} [T_{nj}^{\ell-1}]^{\mathrm{T}}\{A_{k,\ell-1}^n\} = [B_{j,\ell-1}] \sum_{\substack{n=1 \\ n \neq j}}^{N_{\ell-1}} [T_{nj}^{\ell-1}]^{\mathrm{T}} \zeta_k^n \{R_n\}, \quad j = 1 \sim N_{\ell-1}. \tag{33}$$

Then, by considering an outer-field expression of the sum of the forced radiation part plus the scattered interaction part, the radiation potential due to the kth mode of motion of a fictitious body at level ℓ will be obtained. From this, the vector of radiation characteristics of a fictitious body can be derived, with the following result:

$$\{\mathscr{R}_{k,\ell}^i\} = \sum_{j=1}^{N_{\ell-1}} [M_{ji}^{\ell}]^{\mathrm{T}}(\zeta_k^i \{R_j\} + \{A_{k,\ell-1}^j\}). \tag{34}$$

Next, let us proceed to the interactions at the upper level ℓ. The analysis may be undertaken in the same way as that at level $\ell - 1$, and the total incident-wave potential on body i at level ℓ can be written as

$$\varphi^i_{k,\ell} = \sum_{\substack{n=1 \\ n \neq i}}^{N_\ell} (\{\mathscr{R}^n_{k,\ell}\}^{\mathrm{T}} + \{A^n_{k,\ell}\}^{\mathrm{T}})[T^\ell_{ni}]\{\psi^i_{I,\ell}\}. \tag{35}$$

As shown in equation (23), the diffraction characteristics of body i at level ℓ are given by the matrix $[\mathscr{B}_{i,\ell}]$. Hence, simultaneous equations for the vector of interaction coefficients of the kth mode of motion can be obtained in the form

$$\{A^i_{k,\ell}\} - [\mathscr{B}_{i,\ell}] \sum_{\substack{n=1 \\ n \neq i}}^{N_\ell} [T^\ell_{ni}]^{\mathrm{T}}\{A^n_{k,\ell}\} = [\mathscr{B}_{i,\ell}] \sum_{\substack{n=1 \\ n \neq i}}^{N_\ell} [T^\ell_{ni}]^{\mathrm{T}}\{\mathscr{R}^n_{k,\ell}\}, \quad i = 1 \sim N_\ell. \tag{36}$$

It is noteworthy that the matrices of influence coefficients on the left-hand side of equations (21) and (33) are of the same form, and thus can be solved at the same time. The same is true of the simultaneous equations at level ℓ, i.e. equations (19) and (36).

4.3. Hydrodynamic Pressure Force

The radiation potential can be divided into two parts: the first is due to the forced oscillation in the absence of other bodies, and the second one is due to radiated waves from other bodies and reflected waves. The first part is given by equation (31) and the second part may be obtained from equation (32) and a combination of equations (35) and (20). This leads to

$$\Phi^j_k = \zeta^j_k \Phi^j_R + \{\mathscr{A}^j_k\}^{\mathrm{T}}\{\varphi^j_D\}, \tag{37}$$

where

$$\{\mathscr{A}^j_k\}^{\mathrm{T}} = \sum_{\substack{n=1 \\ n \neq j}}^{N_{\ell-1}} (\zeta^n_k\{R_n\}^{\mathrm{T}} + \{A^n_{k,\ell-1}\}^{\mathrm{T}})[T^{\ell-1}_{nj}] + \sum_{\substack{n=1 \\ n \neq i}}^{N_\ell} (\{\mathscr{R}^n_{k,\ell}\}^{\mathrm{T}} + \{A^n_{k,\ell}\}^{\mathrm{T}})[T^\ell_{ni}]\left([I^{\ell-1}_{ij}] + \sum_{\substack{n=1 \\ n \neq j}}^{N_{\ell-1}} [A^n_{S,\ell-1}][T^{\ell-1}_{nj}]\right). \tag{38}$$

Therefore, the hydrodynamic pressure force in the mth mode due to a superposition of all radiation modes can be computed as

$$-\iint_{S_H} p_R\, n_m \,\mathrm{d}S = -\rho g A K \sum_{k=1}^{\infty}\left(\frac{X_k}{A}\right)\sum_{j=1}^{N_B}\iint_{S_j} \Phi^j_k\, \zeta_m(x, y)\, n_z \,\mathrm{d}S \equiv \rho g A K \sum_{k=1}^{\infty}\left(\frac{X_k}{A}\right) F_{mk}. \tag{39}$$

Here F_{mk} can be given by substituting equation (37) and then using equations (13) and (29), with the result

$$F_{mk} = \sum_{j=1}^{N_B} \zeta^j_m[\,\zeta^j_k(A^j_{zz} - \mathrm{i}\,B^j_{zz}) - \{\mathscr{A}^j_k\}^{\mathrm{T}}\{E^j_z\}]. \tag{40}$$

Here again $\zeta_m(x, y)$ has been assumed constant over the bottom of each cylinder, and represented by $\zeta_m(x_j, y_j) = \zeta_m^j$.

4.4. Hydrostatic Pressure Force

Variation of the static pressure due to the deck motion can be expressed by

$$p_S = \rho g w = \rho g A \sum_{k=1}^{\infty} \left(\frac{X_k}{A} \right) \zeta_k(x, y). \tag{41}$$

Thus, the resulting force in the mth mode can be analytically computed as

$$- \iint_{S_H} p_S \, n_m \, \mathrm{d}S = - \rho g A \sum_{k=1}^{\infty} \left(\frac{X_k}{A} \right) C_{mk}. \tag{42}$$

Here

$$C_{mk} \simeq A_W \sum_{j=1}^{N_B} \zeta_m^j \, \zeta_k^j, \tag{43}$$

and A_W denotes the water-plane area, which is given by πa^2 for a hemisphere or circular cylinder.

5. MOTIONS OF AN ELASTIC DECK

The equation of motion of a thin plate is given as

$$- m_B \omega^2 w(x, y) + D \nabla^4 w(x, y) = - p(x, y), \tag{44}$$

where m_B is the distribution of mass, which is equal to M/LB in the case of uniform distribution (M being the total mass), D is the flexural rigidity given by $D = EI/(1 - \nu^2)$, with EI and ν being the equivalent stiffness factor and Poisson's ratio, respectively, and $\nabla = (\partial/\partial x, \partial/\partial y)$ is the 2-D differential operator. Despite a great number of columns being attached beneath the upper deck, it is assumed that the plate is isotropic and the flexural rigidity is constant; this is just for simplicity of the analysis.

Since the structure is freely floating, the bending moment and the equivalent shear force must be zero along the edge of the plate. That is,

$$\frac{\partial^2 w}{\partial n^2} + \nu \frac{\partial^2 w}{\partial s^2} = 0, \quad \frac{\partial^3 w}{\partial n^3} + (2 - \nu) \frac{\partial^3 w}{\partial n \partial s^2} = 0, \tag{45}$$

where n and s denote the normal and tangential directions, respectively. In the case of a rectangular plate, a concentrated force, stemming from replacement of the torsional moment with an equivalent shear force, acts at the four corners, and this must also be zero:

$$R_f = 2D(1 - \nu) \frac{\partial^2 w}{\partial x \partial y} = 0 \quad \text{at } x = \pm 1, \, y = \pm b. \tag{46}$$

Substituting equation (4) into equation (44), multiplying both sides by the normal component of the mth modal function, $n_m = \zeta_m(x, y) \, n_z; m = 1, 2, \ldots, \infty$, and integrating over the structure, we obtain a linear set of equations

$$\sum_{k=1}^{\infty} \left(\frac{X_k}{A} \right) [-K(M' \delta_{mk} + F_{mk}) + C_{mk} + D' S_{mk}] = E_m, \tag{47}$$

where $M' = M/2\rho L^3$ and $D' = D/\rho g(L/2)^4$; δ_{mk} denotes the Kronecker delta, equal to 1 when $m = k$ and zero otherwise. F_{mk}, C_{mk}, and E_m are pressure forces, and these are given by equations (40), (43), and (26), respectively. S_{mk} is the stiffness matrix, corresponding to the restoring force due to the structural rigidity.

Up to this point, the free-end conditions (45) and (46) have not been explicitly imposed as constraints on the solution. However, as shown in Kashiwagi (1998), these conditions can be satisfied as natural boundary conditions in the process of transforming S_{mk} by partial integrations. The final form of S_{mk} to be used in equation (47) is expressed as

$$S_{mk} = \iint_{S_H} \nabla^2\zeta_m \nabla^2\zeta_k \,\mathrm{d}x\,\mathrm{d}y + (1-\nu)\int_{-1}^{1}\left[\frac{\partial\zeta_m}{\partial x}\frac{\partial^2\zeta_k}{\partial x\partial y} - \frac{\partial\zeta_m}{\partial y}\frac{\partial^2\zeta_k}{\partial x^2}\right]_{-b}^{b}\mathrm{d}x + (1-\nu)\int_{-b}^{b}\left[\frac{\partial\zeta_m}{\partial y}\frac{\partial^2\zeta_k}{\partial x\partial y} - \frac{\partial\zeta_m}{\partial x}\frac{\partial^2\zeta_k}{\partial y^2}\right]_{-1}^{1}\mathrm{d}y. \tag{48}$$

Since the present modal functions are expressed in closed form, all integrals shown above can be evaluated analytically.

6. RESULTS AND DISCUSSION

6.1. Accuracy and Convergence Check

Numerical accuracy and convergence are checked for a square array of half-immersed spheres with 64 total elements. As shown in Figure 3, 16 bodies in each quadrant are periodically placed with a half-spacing $s/a = 2{\cdot}0$, but each group of 16 bodies is separated on opposite sides of the x- and y-axis by double the distance between adjacent bodies inside

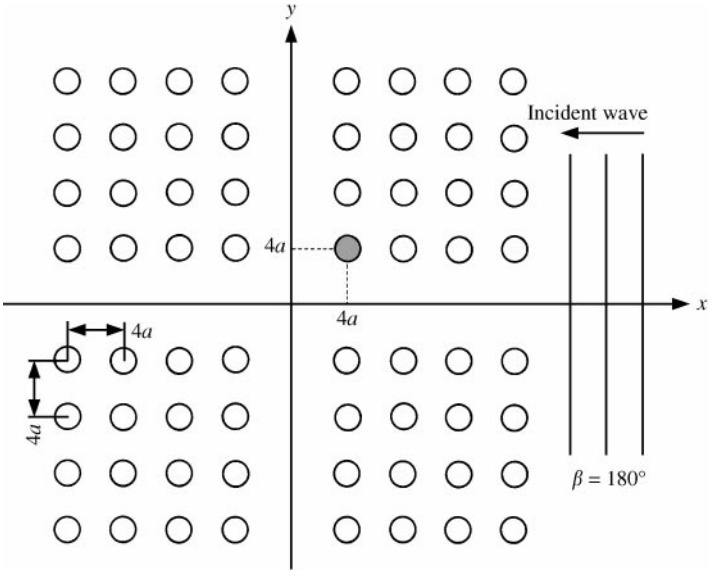

Figure 3. Arrangement of 64 half-immersed spheres.

TABLE 1

Amplitude of wave exciting forces in surge (E_x) and heave (E_z) on a body at $(x, y) = (4a, 4a)$, and the average of total heave force on 64 half-immersed spheres; $h/a = 3{\cdot}0$, $Ka = 0{\cdot}5$, $\beta = 180^\circ$, $s/a = 2{\cdot}0$

No. of terms		$\lvert E_x\rvert$	$\lvert E_z\rvert$	$\lvert\sum E_z\rvert/N_B$
Hierarchical interaction theory (*level* = 3)				
$N = 0$	$M = 12$	0·36597	0·70835	0·07340
	$M = 14$	0·36579	0·70830	0·07339
	$M = 16$	0·36576	0·70828	0·07339
$N = 1$	$M = 12$	0·36576	0·70923	0·07306
	$M = 14$	0·36557	0·70918	0·07305
	$M = 16$	0·36552	0·70916	0·07305
$N = 2$	$M = 14$	0·36558	0·70918	0·07305
Kagemoto & Yue's theory (*level* = 1)				
$N = 0$	$M = 3$	0·36574	0·70828	0·07339
	$M = 4$	0·36574	0·70828	0·07339
$N = 1$	$M = 4$	0·36550	0·70916	0·07305
$N = 2$	$M = 3$	0·36552	0·70916	0·07305

TABLE 2

Added-mass and damping coefficients in heave of a body at $(x, y) = (4a, 4a)$, and the average of total heave added mass of 64 half-immersed spheres; $h/a = 3{\cdot}0$, $Ka = 0{\cdot}5$, $\beta = 180^\circ$, $s/a = 2{\cdot}0$

No. of terms		A_{33}	B_{33}	$\sum A_{33}/N_B$
Hierarchical interaction theory (*level* = 3)				
$N = 0$	$M = 12$	0·81751	0·29999	0·57249
	$M = 14$	0·81769	0·30000	0·57249
	$M = 16$	0·81764	0·30002	0·57246
$N = 1$	$M = 12$	0·82197	0·29881	0·59962
	$M = 14$	0·82216	0·29882	0·59961
	$M = 16$	0·82211	0·29884	0·59958
$N = 2$	$M = 14$	0·82216	0·29882	0·59961
Kagemoto & Yue's theory (*level* = 1)				
$N = 0$	$M = 3$	0·81763	0·30003	0·57244
	$M = 4$	0·81764	0·30003	0·57246
$N = 1$	$M = 4$	0·82211	0·29885	0·59958
$N = 2$	$M = 3$	0·82211	0·29885	0·59963

the group. The water depth is taken as $h/a = 3{\cdot}0$, and head waves ($\beta = 180^\circ$) with wavenumber $Ka = 0{\cdot}5$ are selected as an example. Tables 1 and 2 show the results of the diffraction and radiation problems, respectively; listed are the forces on a body at $(x, y) = (4a, 4a)$, as depicted in Figure 3, and the average of the forces on all 64 bodies.

The hierarchical interaction theory is tested with the highest level set to $\ell = 3$, in which 2×2 bodies are grouped at each level. Computed results are compared with the

corresponding results based on Kagemoto & Yue's (1986) interaction theory. In both tables, N denotes the number of evanescent modes and M is the number of terms in the azimuthal angle in equations (9) and (12). The wave-exciting forces are nondimensionalized with $\rho g A(\pi a^2)$, and the added-mass and damping coefficients are nondimensionalized with $\rho \nabla$ and $\rho \nabla \omega$, respectively, where $\nabla = 2\pi a^3/3$.

By comparison with the results of Kagemoto & Yue's theory, the present hierarchical theory gives converged results to four decimal places with $M = 14$. The need for the larger number of terms in M is caused by slow convergence of the multipole expansion, shown as equation (B.4) in Appendix B. Nevertheless, the computation time is small; for example, only 6 s are needed for the case of $N = 0$ and $M = 14$, using a C200 model of HP workstation. Another thing to be noted is that the contributions of evanescent modes are small, and practically those effects may be ignored.

In the present computations, the diffraction and radiation characteristics of a single body are computed by means of a higher-order boundary element method with 9-point Lagrangian elements (Kashiwagi & Kohjoh 1995). Furthermore, double symmetries with respect to the x- and y-axis are exploited, which can reduce the number of unknowns to $\frac{1}{4}$.

6.2. Responses of a Column-Supported VLFS

Computations were performed for a practical number of columns, which are identical, equally-spaced, and attached beneath a thin rectangular deck of $L = 1{,}200$ m and $B = 240$ m.

The principal particulars of this structure are shown in Table 3. The elementary column considered here is a truncated circular cylinder and the numbers of columns are 1280, 2880, and 5120. In computations of these, 2×2 cylinders are grouped as one unit at the first and second levels in the hierarchical theory. At the highest level ($\ell = 3$), double symmetries with respect to the x- and y-axis are effectively used, which reduces the number of unknowns and thus the computation time. Despite the increase of column numbers, the displacement volume is kept constant by decreasing only the diameter. (Thus the draft and the separation ratio are unchanged and the water-plane area is also the same.)

Figure 4 shows a snap shot taken at $t = 0$ (real part) of the deflection of Model A ($N_B = 1280$) in a regular head wave ($\beta = 0^\circ$) of $L/\lambda = 10$. (λ is the wavelength in deep water given by $2\pi g/\omega^2$.) The numbers of evanescent wave and progressive wave modes are taken as $N = 0$ and $M = 12$, respectively. It should be noted that perfect convergence as in

Table 3

Principal particulars of column-supported structures used in calculations

	Model A	Model B	Model C
Length (L)		1200 m	
Width (B)		240 m	
Flexural rigidity		$D = 1{\cdot}0 \times 10^{10}$ N m	
Poisson's ratio		$\nu = 0{\cdot}3$	
Number of columns (N_B)	16×80 $= 1280$	24×120 $= 2880$	32×160 $= 5220$
Diameter of each column ($2a$)	7·5 m	5·0 m	3·75 m
Draft of each column (d)		3·75 m	
Separation ratio (s/a)		2·0	
Water depth (h)		18·75 m ($h/d = 5{\cdot}0$)	

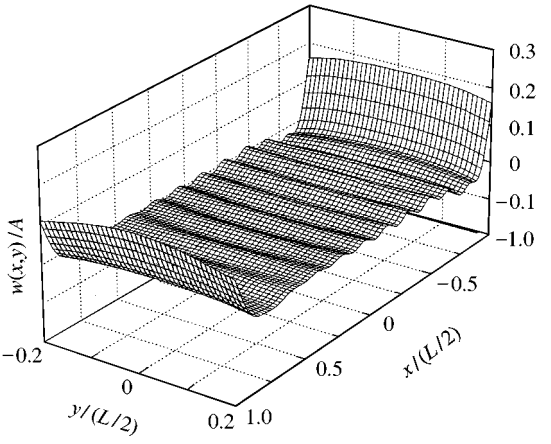

Figure 4. Real part of the deflection of Model A ($N_B = 1280$) in head wave of $L/\lambda = 10$.

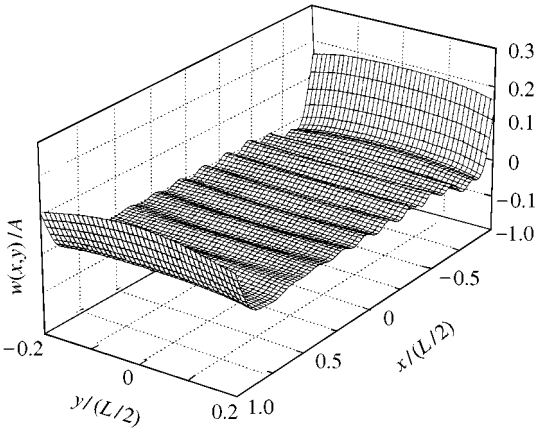

Figure 5. Real part of the deflection of Model C ($N_B = 5120$) in head wave of $L/\lambda = 10$.

Tables 1 and 2 is not achieved in the present case, probably because a fictitious cylinder at level 3 overlaps slightly with adjacent fictitious cylinders. However, the error caused by this is believed to be negligibly small; a similar problem was discussed by Yoshida *et al.* (1993). In fact, it is confirmed that the results including the first evanescent mode ($N = 1$) are virtually the same as Figure 4 and the difference was not discernable in the figures.

Regarding the effect of increasing the number of modal functions, very good convergence is confirmed. To be on the safe side, modal functions in equation (4) are taken up to $m = 20$ and $n = 5$, which are much larger than necessary.

The deflection of a deck is strongly influenced by the rigidity, but compared to a pontoon-type VLFS studied by Kashiwagi (1998), the deflection looks small in the middle part and relatively large in the downwave end of the plate.

Figure 5 is the result for Model C ($N_B = 5120$) in the same waves as that for Figure 4; i.e. $L/\lambda = 10$ in head waves. Evanescent wave modes are not included, and the number of progressive wave modes is taken as $M = 12$, which is also the same as in Figure 4.

Surprisingly, computed deflection patterns are very much the same irrespective of the number of columns. (Although the result for Model B is not shown here, it is confirmed to

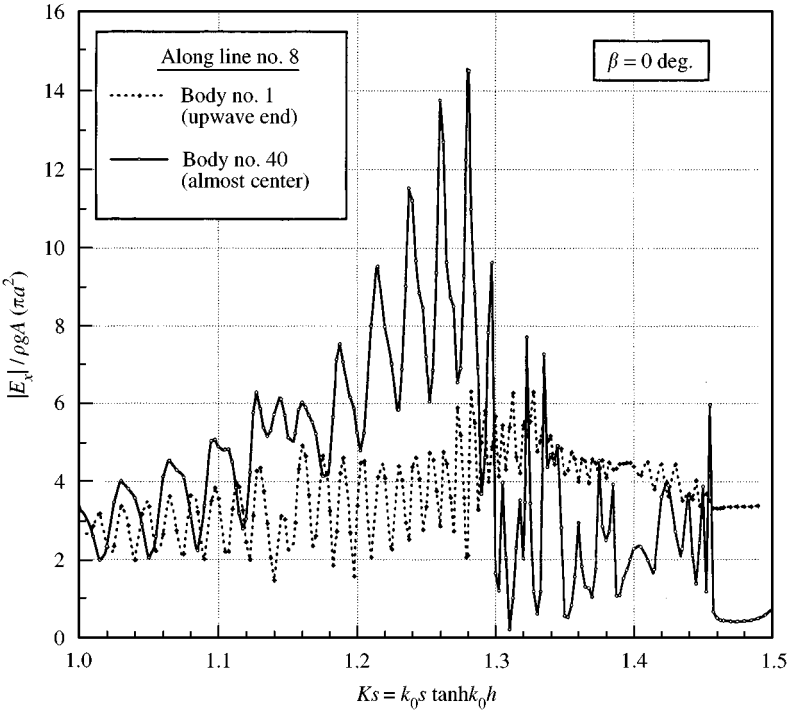

Figure 6. Surge exciting force on bodies No. 1 and No. 40 along row No. 8 of Model A ($N_B = 1280$); $s/a = 2{\cdot}0$, $h/d = 5{\cdot}0$, $d/a = 1{\cdot}0$.

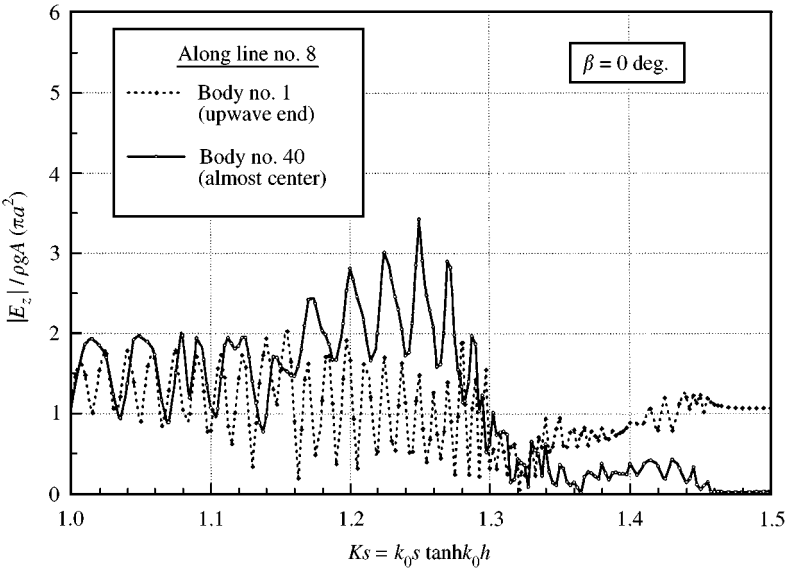

Figure 7. Heave exciting force on bodies No. 1 and No. 40 along row No. 8 of Model A ($N_B = 1280$); $s/a = 2{\cdot}0$, $h/d = 5{\cdot}0$, $d/a = 1{\cdot}0$.

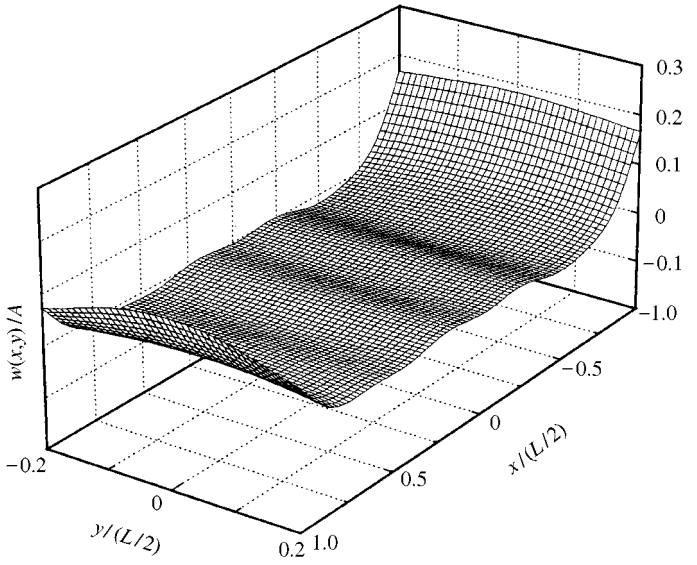

Figure 8. Real part of the deflection of Model A ($N_B = 1280$) in head wave of $L/\lambda = 32{\cdot}59$ ($Ks = 1{\cdot}28$).

be almost the same as in Figures 4 and 5.) In these computations, the wavelength ($L/\lambda = 10$) is large relative to the size of each column, and the displacement volume, flexural rigidity, and water-plane area are exactly the same. Therefore, the deflection pattern may be determined predominantly by the restoring force. However, in short waves whose wavelength is of the same order as the separation distance between neighboring columns, hydrodynamic interactions will be intensified by the so-called trapped-wave phenomenon; this has recently been discussed by Maniar & Newman (1997), Evans & Porter (1997), and Utsunomiya & Eatock Taylor (1998).

To investigate this phenomenon, the wave exciting forces in surge and heave were computed for the two representative cylinders in an array of 1280 cylinders (Model A in Table 3). Figures 6 and 7 show the surge and heave forces, respectively. The dashed line denotes the results on body No. 1 (which is at the upwave end) and the solid line denotes the results on body No. 40 (which is at almost the centre) along row No. 8.

We can see that there are many peaks even within a narrow range of wavenumbers. One distinctive feature is that the surge force acting on a cylinder at almost the centre becomes very large when the wavenumber is slightly less than $Ks \simeq 1{\cdot}3$. The occurrence of these many peaks may be caused by a sequence of Neumann- and Dirichlet-trapped modes to be expected for a large number of equally spaced cylinders.

The wavenumber corresponding to $L/\lambda = 10$, adopted in Figure 4, is $Ks = 0{\cdot}393$, which is far left of Figures 6 and 7 and thus the interactions are expected to be small.

As an example for resonant hydrodynamic interactions, the deflection pattern of Model A was computed at $Ks = 1{\cdot}28$, and the result is shown in Figure 8. $Ks = 1{\cdot}28$ corresponds to $L/\lambda = 32{\cdot}59$, and the numbers of modal functions for this case are taken up to $m = 30$ and $n = 6$ in the x- and y-direction, respectively.

Compared to a longer-wave case of $L/\lambda = 10$ shown in Figure 4, the deflection amplitude remains small. However, the wavelength in the structural deflection becomes long, in spite of a shorter incident wave. A possible reason of this counter-intuitive phenomenon is as follows: in this particular short wave, the hydrodynamic interaction forces may be more

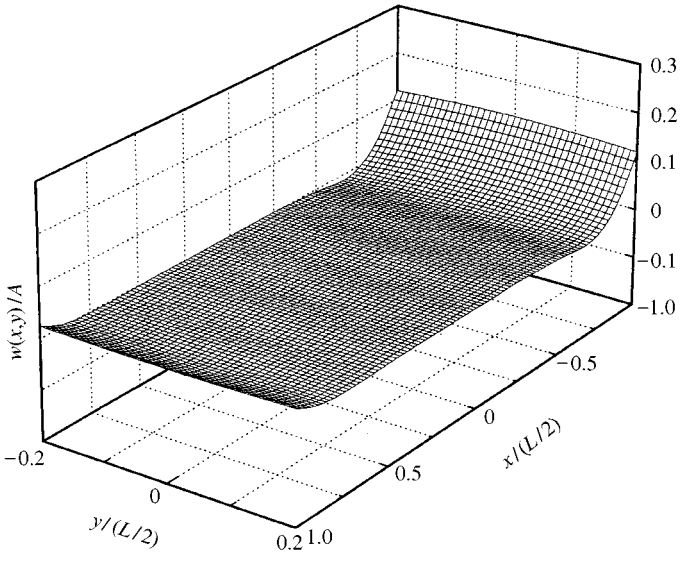

Figure 9. Real part of the deflection of Model C ($N_B = 5120$) in head wave of $L/\lambda = 32{\cdot}59$ ($Ks = 0{\cdot}64$).

dominant than the restoring force, and the spatial distribution of interaction forces is similar to the deflection pattern shown in Figure 8. It is noteworthy that the vertical deflection is caused by the vertical exciting force alone and not connected with the horizontal surge force. At $Ks = 1{\cdot}28$, judging from Figure 7, the vertical exciting force may not be large and this is a reason for the small deflection.

To check the effect of resonant interactions, computations were also performed for Model C (5120 cylinders) at the same wavelength. Since the radius of an elementary cylinder in Model C is half the radius of that in Model A and s/a is unchanged, the nondimensional wavenumber is $Ks = 0{\cdot}64$ for Model C. At this wavenumber, the variation of the wave field may be different from that in Model A. In fact, the deflection pattern of Model C shown in Figure 9 is different from that of Model A and almost zero except near the upwave end.

6.3. Wave Pattern Around Column-Supported VLFS

In connection with trapped waves, the wave pattern is one of the great interests for the case of a large number of cylinders. Waves outside a structure can be computed in terms of the scattered and radiation potentials at the highest level, with the result

$$\frac{\zeta(x, y)}{A} = \Phi_I(x, y) + \sum_{j=1}^{N_\ell} \left[\{A^j_{S,\ell}\}^{\mathrm{T}} \{\psi^j_{S,\ell}\} - K \sum_{k=1}^{\infty} \left(\frac{X_k}{A} \right) (\{\mathscr{R}^j_{k,\ell}\}^{\mathrm{T}} + \{A^j_{k,\ell}\}^{\mathrm{T}}) \{\psi^j_{S,\ell}\} \right], \quad (49)$$

where Φ_I is given by equation (2) and other coefficients and functions are already determined in Sections 3 and 4.

Firstly, the wave pattern at $L/\lambda = 10$ is shown in Figure 10. It is confirmed that this pattern is the same irrespective of the number of columns and that the effects of evanescent waves and structural deflection are also negligibly small. We can see in Figure 10 that the reflection from the bow is small and the wave amplitude along the side of the structure decreases.

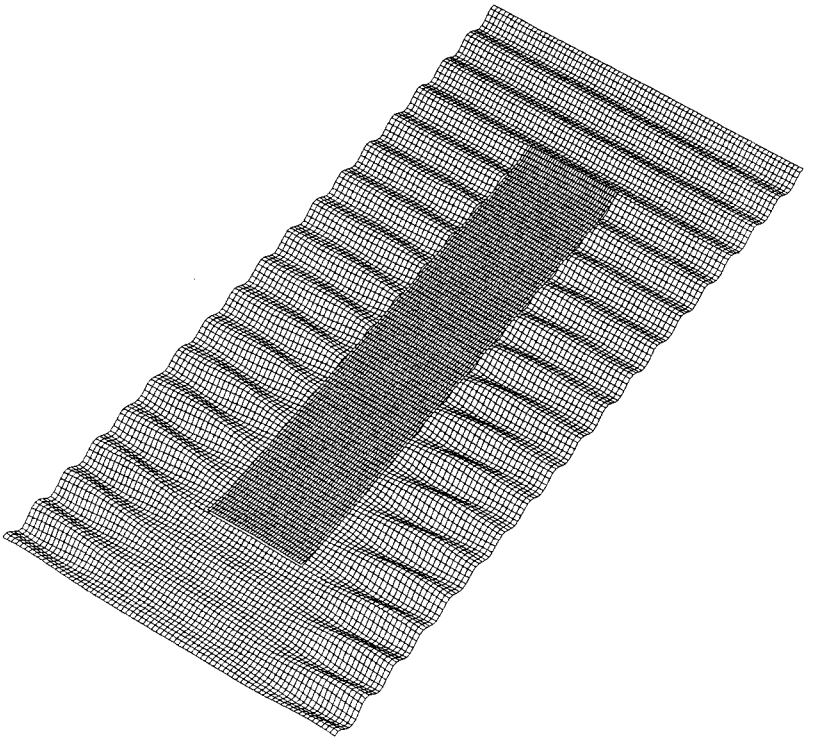

Figure 10. Wave pattern around Model A in head wave of $L/\lambda = 10$, which is the same as those of Models B and C.

Next, the wave pattern at $Ks = 1{\cdot}28$ ($L/\lambda = 32{\cdot}59$) around Model A, comprising 1280 cylinders, is shown in Figure 11. Likewise, Figure 12 shows the wave pattern around Model C (5120 cylinders) at the same wavenumber. In order to elucidate the wave height along the longitudinal side, the structural deflection on the deck is not shown.

Interestingly, the amplitude increases along the longitudinal side in Model A and there exist resonant waves whose crest line is almost perpendicular to that of the incident wave. These facts are connected with trapped waves among a great number of cylinders. In Model C, large amplitude waves still exist downstream of the structure, but the wave pattern is markedly different from that of Model A.

7. CONCLUSIONS

By using a newly developed hierarchical interaction theory, column-supported-type VLFSs were studied, with emphasis placed on hydrodynamic interactions among a large number of columns. Three different numbers of equally spaced circular cylinders were considered as supporting columns; these were 1280, 2880, and 5120 cylinders, but the total displacement volumes and water-plane areas were kept constant.

In the results for $L/\lambda = 10$, differences in the upper-deck deflection were very small among those three cases. This is probably because the interactions were small at this longer wavelength and the restoring force was dominant in the motion equation.

At shorter wavelengths, resonant phenomena were observed, which may be connected with trapped modes of Neumann and Dirichlet types, studied by Maniar & Newman (1997) for a single row of cylinders. In this wavelength region, the hydrodynamic interaction forces

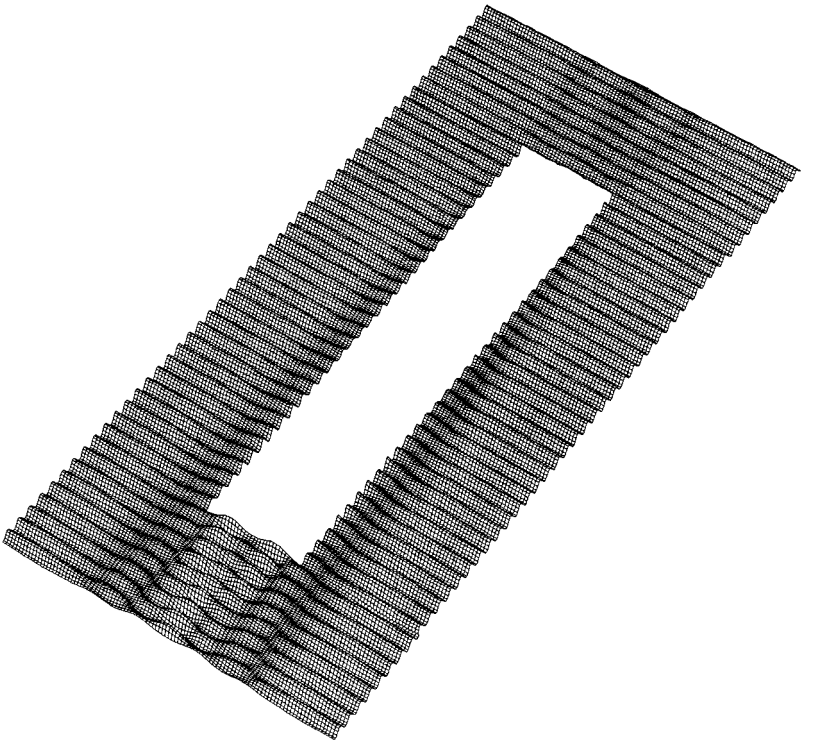

Figure 11. Wave pattern around Model A ($N_B = 1280$) in a wave of $L/\lambda = 32{\cdot}59$ coming from the right upper side.

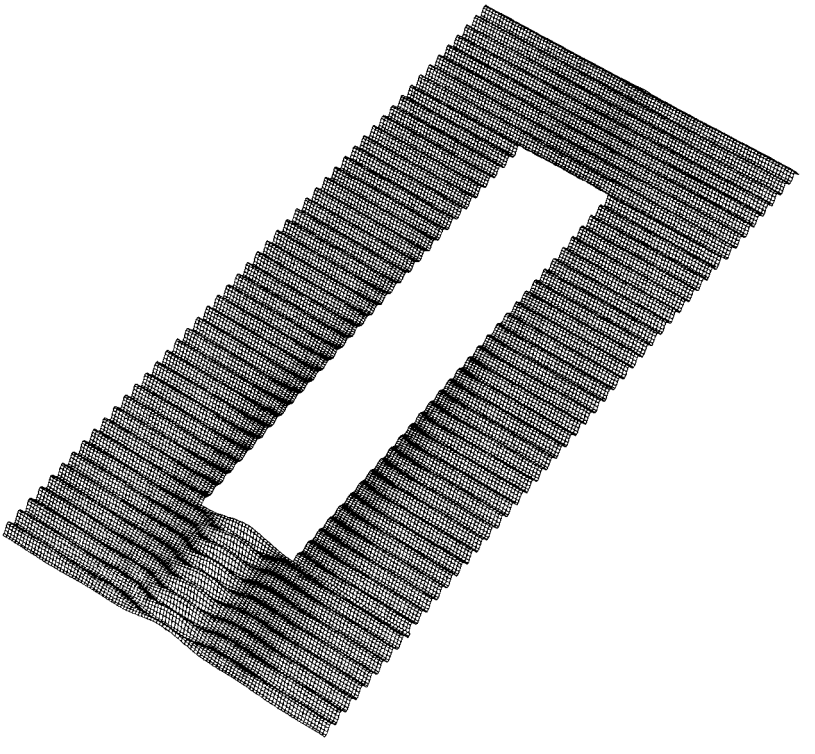

Figure 12. Wave pattern around Model C ($N_B = 5120$) in a wave of $L/\lambda = 32{\cdot}59$ coming from the right upper side.

are more dominant than the restoring force, and the intensity and spatial distribution of the interaction forces vary depending on the ratio of the wavelength to the separation distance between adjacent cylinders. Therefore, as expected, the structural deflection was different between two structures supported by 1280 and 5120 cylinders.

The wave patterns around these two structures were also computed and their distinctive features associated with trapped-wave phenomena were shown in figures.

References

Evans, D. V. & Porter, R. 1997 Near-trapping waves by circular arrays of vertical cylinders. *Applied Ocean Research* **19,** 83–99

Kagemoto, H. & Yue, D. K. P. 1986 Interactions among multiple three-dimensional bodies in water waves: an exact algebraic method. *Journal of Fluid Mechanics* **166,** 189–209

Kagemoto, H. 1995 On the comparisons of behaviours in waves of semisubmersible-type and pontoon-type Very Large Floating Structures. *Proceedings of* 13*th Ocean Engineering Symposium*, Society of Naval Architects of Japan, pp. 231–238

Kashiwagi, M. & Kohjoh, T. 1995 A method of computing hydrodynamic interactions in Large Floating Structures composed of multiple bodies. *Proceedings of* 13*th Ocean Engineering Symposium*, Society of Naval Architects of Japan, pp. 247–254

Kashiwagi, M. 1998 A B-Spline Galerkin scheme for calculating the hydroelastic response of a Very Large Floating Structure in waves. *Journal of Marine Science and Technology* **3,** 37–49

Lin, X. & Takaki, M. 1998 A B-Spline element method for predicting the hydroelastic responses of a Very Large Floating Structure in waves. *Journal of the Society of Naval Architects of Japan* **183,** 219–225

Maniar, H. D. & Newman, J. N. 1997 Wave diffraction by a long array of cylinders. *Journal of Fluid Mechanics* **339,** 309–330

Murai, M., Kagemoto, H. & Fujino, M. 1998 On the predictions of hydroelastic behaviours of a huge floating structure in waves. *Journal of the Society of Naval Architects of Japan* **183,** 199–210

Newman, J. N. 1994 Wave effects on deformable bodies. *Applied Ocean Research* **16,** 47–59

Ohmatsu, S. 1997 Numerical calculation of hydroelastic responses of pontoon type VLFS. *Journal of the Society of Naval Architects of Japan* **182,** 329–340

Utsunomiya, T. & Eatock Taylor, R. 1998 Analogies for resonances in wave diffraction problems. *Proceedings of* 13*th International Workshop on Water Waves and Floating Bodies*, pp. 159–162

Yoshida, K. Suzuki, H., Oka, N., Iijima, K., Shimura, T. & Arima, T. 1993 Hydrodynamic interaction effects on wave exciting force in Large Scale Floating Structures. *Journal of the Society of Naval Architects of Japan* **174,** 243–251

Yoshida, K., Iijima, K., Suzuki, H. & Oka, T. 1994 Hydrodynamic interaction effects on wave exciting force in Large Scale Floating Structures (2nd Report). *Journal of the Society of Naval Architects of Japan* **176,** 185–192

APPENDIX A: DIFFRACTION CHARACTERISTICS

Let us consider the diffraction problem of the jth body in an elementary wave of "generalized" incident-wave vector defined by equation (9), and let the velocity potential of an elementary wave and the corresponding scattered potential be denoted by $\psi_I^j(x, y, z)$ and $\varphi_S^j(x, y, z)$, respectively.

We note that $\psi_I^j(x, y, z)$ satisfies Laplace's equation and the free-surface and bottom conditions. In addition, $\varphi_S^j(x, y, z)$ satisfies the radiation condition at infinity as well. Therefore, we can prove with Green's theorem that the total diffraction potential, $\varphi_D^j = \psi_I^j + \varphi_S^j$, is a solution of the integral equation

$$C(P)\,\varphi_D^j(P) + \iint_{S_j} \varphi_D^j(Q)\,\frac{\partial}{\partial n_Q}\,G(P;\,Q)\,\mathrm{d}S = \psi_I^j(P), \tag{A.1}$$

where $C(P)$ is the solid angle, $P = (x, y, z)$ is the field point, $Q = (x', y', z')$ is the integration point, and $\partial/\partial n_Q$ denotes the normal derivative with the positive normal directed out of the body.

$G(P;Q)$ is the Green function, which can be expressed as

$$G(P;\,Q) = \frac{i}{2}\,C_0 Z_0(z)Z_0(z')\mathrm{H}_0^{(2)}\{k_0\sqrt{(x-x')^2+(y-y')^2}\} + \frac{1}{\pi}\sum_{n=1}^{\infty} C_n Z_n(z)Z_n(z')\mathrm{K}_0\{k_n\sqrt{(x-x')^2+(y-y')^2}\}, \tag{A.2}$$

where

$$C_0 = \frac{k_0^2}{K + h(k_0^2 - K^2)}, \quad C_n = \frac{k_n^2}{K - h(k_n^2 + K^2)}, \tag{A.3}$$

and other notations are defined in equations (3) and (10).

$\mathrm{H}_0^{(2)}$ and K_0 in equation (A.2) are the second kind of Hankel and modified Bessel functions, respectively. These functions can be recast in the series-expansion form by expressing $x + \mathrm{i}y = r\exp(\mathrm{i}\theta)$ and $x' + \mathrm{i}y' = r'\exp(\mathrm{i}\theta')$ and by utilizing the addition theorem of Bessel functions. Considering the case of field point P in the fluid, $C(P) = 1$ and $r > r'$. Therefore, from equations (A.1) and (A.2), we can obtain the following representation of the scattered potential:

$$\varphi_S^j(P) = \sum_{m=-\infty}^{\infty}\left[B_{m0}^j\{Z_0(z)\mathrm{H}_m^{(2)}(k_0 r)\,\mathrm{e}^{-\mathrm{i}m\theta}\} + \sum_{n=1}^{\infty} B_{mn}^j\{Z_n(z)\mathrm{K}_m(k_n r)\,\mathrm{e}^{-\mathrm{i}m\theta}\}\right], \tag{A.4}$$

where

$$B_{m0}^j = -\frac{\mathrm{i}}{2}\,C_0\iint_{S_j}\varphi_D^j(Q)\,\frac{\partial}{\partial n_Q}\,Z_0(z')\mathrm{J}_m(k_0 r')\,\mathrm{e}^{\mathrm{i}m\theta'}\,\mathrm{d}S,$$
$$B_{mn}^j = -\frac{1}{\pi}\,C_n\iint_{S_j}\varphi_D^j(Q)\,\frac{\partial}{\partial n_Q}\,Z_n(z')\mathrm{I}_m(k_n r')\,\mathrm{e}^{\mathrm{i}m\theta'}\,\mathrm{d}S. \tag{A.5}$$

A set of coefficients $\{B_{m0}^j,\ B_{mn}^j\}$ represents the diffraction characteristics corresponding to the elementary wave $\psi_I^j(P)$. By considering the diffraction problems for all elementary waves of $\{\psi_I^j\}$ in the same manner, we can construct the matrix of the diffraction characteristics; this is denoted as $[B_j]^{\mathrm{T}}$ in equation (11).

It should be noted that there is no need to compute the normal velocity of the incident wave in equation (A.1), and the solution of equation (A.1) is the total diffraction potential which can be directly used for computing equation (A.5) and the vector of elementary wave forces defined by equiation (13).

APPENDIX B: GRAF'S ADDITION THEOREM

Summaries are given below of Graf's addition theorems to be used in the hierarchical interaction theory.

In analyzing interactions at the same level, it is necessary to rewrite the scattered potential of body i with a coordinate system fixed at body j. In this case, as shown in Figure B1, $r_j < L_{ij}$ and thus the following relations hold:

$$\mathrm{H}_m^{(2)}(k_0 r_i)\mathrm{e}^{-\mathrm{i}m\theta_i} = \sum_{p=-\infty}^{\infty}\mathrm{H}_{m-p}^{(2)}(k_0 L_{ij})\mathrm{e}^{-\mathrm{i}(m-p)\alpha_{ij}}\{\mathrm{J}_p(k_0 r_j)\mathrm{e}^{-\mathrm{i}p\theta_j}\}, \tag{B.1}$$

$$\mathrm{K}_m(k_n r_i)\mathrm{e}^{-\mathrm{i}m\theta_i} = \sum_{p=-\infty}^{\infty}(-1)^p\mathrm{K}_{m-p}(k_n L_{ij})\mathrm{e}^{-\mathrm{i}(m-p)\alpha_{ij}}\{\mathrm{I}_p(k_n r_j)\mathrm{e}^{-\mathrm{i}p\theta_j}\}, \tag{B.2}$$

where J_p and I_p denote the first kind of Bessel and modified Bessel functions, respectively, and $\mathrm{H}_m^{(2)}$ and K_m are the second kind of Hankel and modified Bessel functions, respectively.

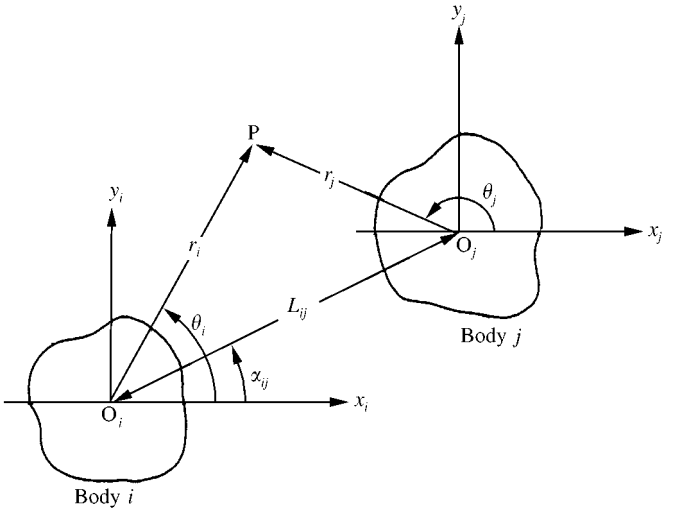

Figure B1. Symbols used in the multiple scattering problem

The above two equations can be expressed in a matrix form

$$\{\psi_S^i(r_i, \theta_i, z)\} = [T_{ij}]\,\{\psi_I^j(r_j, \theta_j, z)\}\,. \tag{B.3}$$

Here $[T_{ij}]$ is the coordinate transformation matrix, and the vectors on the left- and right-hand sides are defined in equations (12) and (9), respectively.

For the case of $r_j > L_{ij}$ in Figure B1, relations (B.1) and (B.2) must be modified, giving the following:

$$\mathrm{H}_m^{(2)}(k_0 r_i)\mathrm{e}^{-\mathrm{i}m\theta_i} = \sum_{p=-\infty}^{\infty} \mathrm{J}_{m-p}(k_0 L_{ij})\mathrm{e}^{-\mathrm{i}(m-p)\alpha_{ij}}\{\mathrm{H}_p^{(2)}(k_0 r_j)\mathrm{e}^{-\mathrm{i}p\theta_j}\}\,, \tag{B.4}$$

$$\mathrm{K}_m(k_n r_i)\mathrm{e}^{-\mathrm{i}m\theta_i} = \sum_{p=-\infty}^{\infty} (-1)^{m-p}\mathrm{I}_{m-p}(k_n L_{ij})\mathrm{e}^{-\mathrm{i}(m-p)\alpha_{ij}}\{\mathrm{K}_p(k_n r_j)\mathrm{e}^{-\mathrm{i}p\theta_j}\}\,. \tag{B.5}$$

These equations can be expressed in the form

$$\{\psi_S^i(r_i, \theta_i, z)\} = [M_{ij}]\,\{\psi_S^j(r_j, \theta_j, z)\}. \tag{B.6}$$

This can be regarded as the multipole expansion of the scattered potential of body i around the origin of the jth coordinate system, and thus $[M_{ij}]$ is called the multipole expansion matrix.

Lastly, let us consider the local expansion of the vector of generalized incident waves around the origin of the jth coordinate system. In this case, the following relations hold for all values of r_j and L_{ij}:

$$\mathrm{J}_m(k_0 r_i)\mathrm{e}^{-\mathrm{i}m\theta_i} = \sum_{p=-\infty}^{\infty} \mathrm{J}_{m-p}(k_0 L_{ij})\mathrm{e}^{-\mathrm{i}(m-p)\alpha_{ij}}\{\mathrm{J}_p(k_0 r_j)\mathrm{e}^{-\mathrm{i}p\theta_j}\}\,, \tag{B.7}$$

$$\mathrm{I}_m(k_n r_i)\mathrm{e}^{-\mathrm{i}m\theta_i} = \sum_{p=-\infty}^{\infty} \mathrm{I}_{m-p}(k_n L_{ij})\mathrm{e}^{-\mathrm{i}(m-p)\alpha_{ij}}\{\mathrm{I}_p(k_n r_j)\mathrm{e}^{-\mathrm{i}p\theta_j}\}\,. \tag{B.8}$$

These can be written in the following form:

$$\{\psi_I^i(r_i, \theta_i, z)\} = [I_{ij}]\,\{\psi_I^j(r_j, \theta_j, z)\}\,. \tag{B.9}$$

Here $[I_{ij}]$ is the local expansion matrix, which is used in the downward transmission of the generalized incident-wave vector in the hierarchical diffraction problem.